



# A super-Chandrasekhar mass type Ia supernova progenitor at 49 pc set to detonate in 23 Gyr

Received: 31 October 2024

Accepted: 10 March 2025

Published online: 04 April 2025

James Munday<sup>1</sup>✉, Ruediger Pakmor<sup>2</sup>, Ingrid Pelisoli<sup>1</sup>,  
David Jones<sup>1,3,4,5</sup>, Snehalata Sahu<sup>1</sup>, Pier-Emmanuel Tremblay<sup>1</sup>,  
Abinaya Swaruba Rajamuthukumar<sup>2</sup>, Gijs Nelemans<sup>1,6,7,8</sup>, Mark Magee<sup>1</sup>,  
Silvia Toonen<sup>9</sup>, Antoine Bédard<sup>1</sup> & Tim Cunningham<sup>1,10</sup>

Check for updates

Double white dwarf binaries are a leading explanation of the origin of type Ia supernovae, but no system exceeding the Chandrasekhar mass limit ( $1.4 M_{\odot}$ ) has been found that will explode anywhere close to a Hubble time. Here we present the super-Chandrasekhar mass double white dwarf WDJ181058.67+311940.94 whose merger time ( $22.6 \pm 1.0$  Gyr) is of the same order as a Hubble time. The mass of the binary is large, combining to  $1.555 \pm 0.044 M_{\odot}$ , while being located only 49 pc away. We predict that the binary will explode dynamically by means of a double detonation that will destroy both stars just before they merge, appearing as a subluminous type Ia supernova with a peak apparent magnitude of about  $m_V = -16$  (200,000 times brighter than Jupiter). The observationally derived birth rate of super-Chandrasekhar mass double white dwarfs is now at least  $6.0 \times 10^{-4} \text{ yr}^{-1}$  and the observed rate of type Ia supernovae in the Milky Way from such systems is approximately  $4.4 \times 10^{-5} \text{ yr}^{-1}$ , whereas the predicted type Ia supernova rate in the Milky Way from all progenitor channels is about sixty times larger. Hence, WDJ181058.67+311940.94 mitigates the observed deficit of massive double white dwarfs witnessed in volume-complete populations, but further evidence is required to determine the majority progenitors of type Ia supernovae.

Binaries comprising at least one white dwarf are the progenitors of type Ia supernovae<sup>1,2</sup>. Type Ia supernovae show an absence of hydrogen in their spectra and are caused by the thermonuclear explosion of a carbon–oxygen white dwarf. Nuclear fusion transforms a substantial amount of, or the entire, white dwarf into heavier elements and ejects them into the interstellar medium. However, the stellar type of the companion to the white dwarf in type Ia progenitors remains largely unclear (see, for example, refs. 3–5).

The substantial population size of double white dwarf binaries has naturally led to them being one of the leading progenitor candidates to explain the abundance of type Ia supernovae<sup>6,7</sup>. These systems form on compact orbits with an orbital period on the timescale of hours to days<sup>8</sup> (orbital separations of hundredths to tenths of astronomical units) following a series of mass transfer events<sup>9</sup>. The gradual loss of orbital angular momentum through gravitational wave radiation draws the two stars closer until the orbital period of massive double

<sup>1</sup>Department of Physics, University of Warwick, Coventry, UK. <sup>2</sup>Max-Planck-Institut für Astrophysik, Garching, Germany. <sup>3</sup>Instituto de Astrofísica de Canarias, La Laguna, Spain. <sup>4</sup>Departamento de Astrofísica, Universidad de La Laguna, La Laguna, Spain. <sup>5</sup>Nordic Optical Telescope, Rambla José Ana Fernández Pérez, Breña Baja, Spain. <sup>6</sup>Department of Astrophysics/IMAPP, Radboud University, Nijmegen, the Netherlands. <sup>7</sup>Institute for Astronomy, KU Leuven, Leuven, Belgium. <sup>8</sup>SRON, Netherlands Institute for Space Research, Leiden, the Netherlands. <sup>9</sup>Anton Pannekoek Institute for Astronomy, University of Amsterdam, Amsterdam, the Netherlands. <sup>10</sup>Center for Astrophysics, Harvard & Smithsonian, Cambridge, MA, USA. ✉e-mail: [james.munday98@gmail.com](mailto:james.munday98@gmail.com)

white dwarfs is a couple of minutes, initiating unstable mass transfer and leading to the demise of the system<sup>10</sup>.

Although many compact double white dwarfs have been discovered on the brink of coalescence (see, for example, refs. 11–13), we have had no direct evidence that these systems exist in nearby, volume-complete populations<sup>14–16</sup>, which casts doubt on whether double white dwarfs can account for a large percentage of the observed type Ia supernova rates. Current synthetic models of the population indicate that super-Chandrasekhar mass limit double white dwarfs are indeed suspected to be scarce<sup>17–19</sup>. However, based on the models of ref. 17 we expect about 150 compact double white dwarf binaries to have total masses that exceed  $1.5 M_{\odot}$  within 100 pc, about one quarter of which merge in under a Hubble time. There has been only one super-Chandrasekhar mass double white dwarf binary discovered (NLTT 12758) (ref. 20), but its 1.15 d period means that the two stars will come into contact in about 10 Hubble times. There are a handful of other candidate subluminous type Ia progenitors that are double white dwarfs that have total masses smaller than the Chandrasekhar mass limit (see, for example, refs. 21–26), two white dwarf+hot subdwarf systems that exceed  $1.4 M_{\odot}$  and have an impending supernova fate<sup>27,28</sup>, and one other white dwarf+hot subdwarf that is also a strong candidate<sup>29,30</sup>.

Growing observational evidence supports hot subdwarfs as some of the products of binary evolution<sup>31</sup>, but, although more super-Chandrasekhar mass systems have been discovered, the binaries much less densely populate the Galaxy<sup>32</sup>. The observed rate of type Ia supernovae initiated from the white dwarf+hot subdwarf channel is expected to be at least  $(1.5–7) \times 10^{-5} \text{ yr}^{-1}$  (ref. 27), whereas the rate of type Ia supernovae in the Galaxy from all progenitors is about  $2.8 \pm 0.6 \times 10^{-3} \text{ yr}^{-1}$  (refs. 4,19,33,34) as inferred through observations of explosions in other galaxies of similar redshift. Multiple other evolutionary scenarios have been suggested as causes for normal and peculiar type Ia supernovae<sup>4</sup> having different companion compositions, but the extent to which they contribute towards the missing fraction of type Ia supernovae is unclear. This ambiguity on the nature of type Ia progenitors is cosmologically problematic. A primary reason is that, until we confirm the leading progenitors of a type Ia supernova, systematic errors in the distances derived to other galaxies could lead to inaccurate measurements, which is particularly troublesome for galaxies at high redshifts<sup>34,35</sup>. In addition, the details of the ejecta velocity and its constituents are important for star formation<sup>36</sup> and the dynamics of gas in galaxies<sup>37</sup>. Not only does the discovery of a local, compact, super-Chandrasekhar mass double white dwarf have the ability to resolve the dearth of systems in the observed sample, but a sample of such systems has the power to reduce the uncertainty of this cosmologically fundamental event.

## Results and discussion

### Physical and orbital properties of WDJ181058.67+311940.94

WDJ181058.67+311940.94 was first discovered as part of the DBL survey<sup>26</sup> which searches for double-lined double white dwarfs using medium-resolution spectra ( $R \approx 8,000–9,000$ ). Fits to these identification spectra indicated the source to be a double white dwarf binary with a high total mass. Afterwards, we launched an observational campaign to acquire time-series spectroscopy of the source to confirm the masses derived through the atmospheric parameters and resolve the orbital period. We obtained phase-resolved radial velocities of WDJ181058.67+311940.94 with the following instruments and telescopes: the Intermediate-dispersion Spectrograph and Imaging System (ISIS) on the 4.2 m William Herschel Telescope (WHT); the Intermediate Dispersion Spectrograph (IDS) on the 2.5 m Isaac Newton Telescope; the Fibre-fed Echelle Spectrograph (FIES) and Alhambra Faint Object Spectrograph and Camera (ALFOSC) on the 2.56 m Nordic Optical Telescope (NOT); and a continuous observing window of 4.5 h using the UV-Visual Echelle Spectrograph (UVES) on the 8.2 m Very Large Telescope (VLT).

**Table 1 | The atmospheric parameters for each spectroscopic dataset**

Telescope/instrument	VLT/UVES	WHT/ISIS	HST/COS	Adopted
$T_{\text{eff},1}$ (K)	$17,230 \pm 710$	$16,500^{+400}_{-300}$	$18,630 \pm 80$	$17,260^{+1,380}_{-880}$
$\log g_1$ (dex)	$8.408 \pm 0.027$	$8.35 \pm 0.05$	$8.307 \pm 0.020$	$8.350^{+0.066}_{-0.052}$
$M_1 (M_{\odot})$	$0.871 \pm 0.018$	$0.83 \pm 0.03$	$0.810 \pm 0.013$	$0.834 \pm 0.039$
$T_{\text{eff},2}$ (K)	$20,190 \pm 280$	$20,200 \pm 300$	$18,010 \pm 70$	$2,0000^{+400}_{-2000}$
$\log g_2$ (dex)	$8.151 \pm 0.021$	$8.16 \pm 0.04$	$8.178 \pm 0.018$	$8.164^{+0.027}_{-0.030}$
$M_2 (M_{\odot})$	$0.713 \pm 0.014$	$0.72 \pm 0.03$	$0.727 \pm 0.013$	$0.721 \pm 0.020$
$M_T (M_{\odot})$	$1.584 \pm 0.022$	$1.55 \pm 0.04$	$1.537 \pm 0.018$	$1.555 \pm 0.044$

Hybrid fitting was performed in all cases using Panoramic Survey Telescope and Rapid Response System (Pan-STARRS) photometry. A systematic difference between the ultraviolet spectroscopy and the optical photometry was considered in the fitting (Methods). Masses are inferred by interpolation of evolutionary sequences<sup>61</sup> and  $M_T$  is the total mass of the system. The final adopted values were obtained by concatenating the distributions obtained for each parameter to quote the median and 68% confidence interval on the  $T_{\text{eff}}$  and  $\log g$ , and then interpolating to find masses. The more/less massive star is labelled with subscript 1/2, respectively. The WHT/ISIS solution is quoted from a previous result<sup>26</sup>.

The UVES data was used for an improved accuracy of the atmospherically derived masses from spectral fits because of its full visible coverage. Precise radial velocity measurements of the target were simultaneously obtained and with this an unambiguous determination of the orbital period. As a further test for consistency of the atmospheric solution with a unique dataset, we also fitted a two-star solution to a previously published Hubble Space Telescope (HST) Cosmic Origins Spectrograph (COS) spectrum<sup>38</sup>. The resultant stellar parameters found by fitting each dataset are quoted in Table 1 and spectral fits to the optical and ultraviolet data are plotted in Fig. 1. Considering the measurements from all datasets, we find stellar parameters of  $T_{\text{eff},1} = 17,260^{+1,380}_{-880}$  K,  $\log g_1 = 8.350^{+0.066}_{-0.052}$  dex,  $M_1 = 0.834 \pm 0.039 M_{\odot}$  for the primary (more massive) star and  $T_{\text{eff},2} = 20,000^{+400}_{-2000}$  K,  $\log g_2 = 8.164^{+0.027}_{-0.030}$  dex,  $M_2 = 0.721 \pm 0.020 M_{\odot}$  for the secondary (less massive) star, leading to a total system mass of  $M_T = 1.555 \pm 0.044 M_{\odot}$ .  $T_{\text{eff}}$ ,  $\log g$  and  $M$  refer to the effective temperature, the surface gravity and the mass of each component, respectively.

All other data was used exclusively for radial velocity measurements at H $\alpha$  to precisely quantify the motion of the stars across all orbital phases and to improve the precision of the period. A Lomb–Scargle periodogram of all radial velocity measurements, which was optimized for physical limits of the system, revealed one clear peak representing the orbital period. The binary parameters are quoted in Table 2 and our phase-folded radial velocity (RV) curve with the best-fit orbital solution is depicted in Fig. 2. The best-fitting orbital parameters were orbital period  $P = 14.23557 \pm 0.00002$  h, semi-amplitudes  $K_1 = 93.9 \pm 2.0$  km s $^{-1}$  and  $K_2 = 95.7 \pm 2.1$  km s $^{-1}$ , and velocity offsets  $\gamma_1 = 50.0 \pm 1.5$  km s $^{-1}$  and  $\gamma_2 = 53.5 \pm 1.6$  km s $^{-1}$ . Being double lined, the mass ratio was independently solvable without knowledge of the orbital inclination using  $q = M_2/M_1 = K_1/K_2$ , such that the orbitally derived value was  $q = 0.98 \pm 0.03$ . This result is in best agreement with the star masses derived from the HST/COS spectrum, which was  $q = 0.90 \pm 0.02$ . Our derived masses from the VLT/UVES spectra yielded a lower  $q = 0.82 \pm 0.02$ , with the mass of the less massive star being near identical to the ultraviolet, and the adopted value, taking into account all measurements, indicated a mass ratio of  $q = 0.86 \pm 0.04$ . The surface gravity of the hotter, less massive star was nearly identical across fits to all datasets. This is unsurprising given that it contributes more flux than the cooler white dwarf, whereas its temperature difference between the ultraviolet and optical datasets primarily arises from the fitting of the slope of the spectral energy distribution across the ultraviolet. Forcing the orbitally derived  $q = 0.98 \pm 0.03$  in the atmospheric fit led to an increase in the surface gravity of the secondary and a decrease

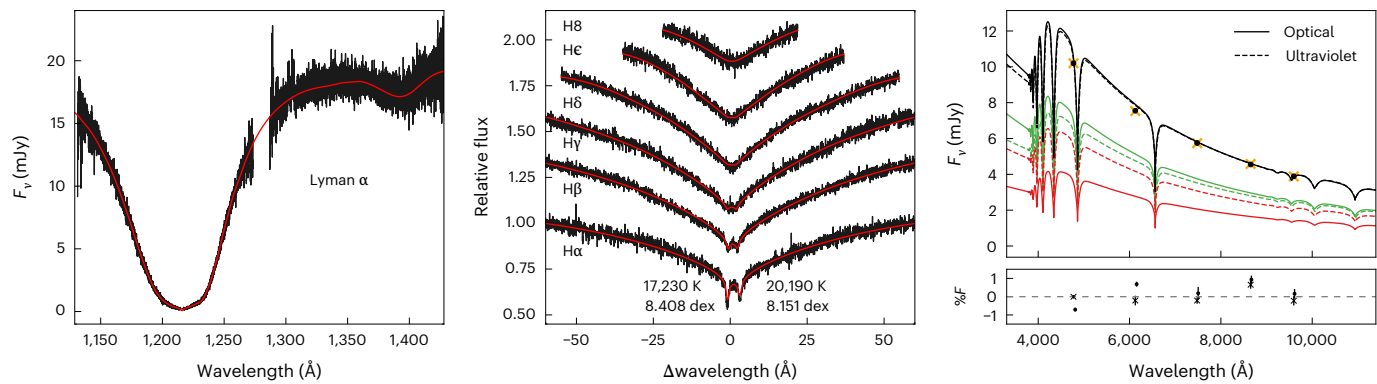


**Fig. 1 | Atmospheric fits to the photometric and spectroscopic datasets.** Left, the HST/COS ultraviolet spectrum with the synthetic spectrum from the hybrid HST/COS with Pan-STARRS photometry fit for a two-star model overlaid in red. The corresponding atmospheric parameters of the DA white dwarfs are  $T_{\text{eff},1} = 18,630$  K,  $\log g_1 = 8.307$  dex,  $T_{\text{eff},2} = 18,010$  K,  $\log g_2 = 8.178$  dex. Middle, a single UVES spectrum from H $\alpha$  to H $8$  with the synthetic spectral model for atmospheric parameters  $T_{\text{eff},1} = 17,230$  K,  $\log g_1 = 8.408$  dex,  $T_{\text{eff},2} = 20,190$  K,  $\log g_2 = 8.151$  dex, overplotted in red. We remind the reader that all Balmer lines up to H $11$  were fitted but are omitted from the plot for clarity. Right, the observed

fluxes in Pan-STARRS (black circles) and the synthetic photometry in each filter for the same atmospheric parameters (orange crosses). The percentage flux residual between the data and the combined flux is found below. The fluxes contributed from the more massive (red) and less massive (green) stars are included for the ultraviolet (dashed) and optical (solid line) fits. The Gaia parallax measurement with a Gaussian prior was an independent variable to scale the observations from an Eddington to an absolute flux perceived in the Solar System.

**Table 2 | Positional, atmospheric and orbital parameters for WDJ181058.67+311940.94**

Parameter	Unit	Value	Uncertainty
Right ascension	deg (2016)	272.744360834	$\pm 0.000000005$
Declination	deg (2016)	31.327961071	$\pm 0.000000005$
Reference epoch	HJD (UTC)	2,458,587.6663	$\pm 0.0018$
Orbital period	day	0.5931479	$\pm 0.0000009$
Gaia parallax	mas	20.438	$\pm 0.023$
Fitted parallax	mas	20.402	$\pm 0.003$
Primary temperature	K	17,260	$+1,380/-880$
Secondary temperature	K	20,000	$+400/-2,000$
Primary surface gravity	dex	8.350	$+0.066/-0.052$
Secondary surface gravity	dex	8.164	$+0.027/-0.030$
Primary mass	$M_{\odot}$	0.834	$\pm 0.039$
Secondary mass	$M_{\odot}$	0.721	$\pm 0.020$
System mass	$M_{\odot}$	1.555	$\pm 0.044$
Primary semi-amplitude	$\text{km s}^{-1}$	93.9	$\pm 2.0$
Secondary semi-amplitude	$\text{km s}^{-1}$	95.7	$\pm 2.1$
Primary velocity offset	$\text{km s}^{-1}$	50.0	$\pm 1.5$
Secondary velocity offset	$\text{km s}^{-1}$	53.5	$\pm 1.6$
Merger time	Gyr	22.6	$\pm 1.0$

The primary and secondary stars correspond to the more massive and less massive components, respectively. The temperatures, surface gravities and masses quoted are the adopted values from the spectroscopic fits, which were determined by considering data from all sources (Table 1).

in the surface gravity of the primary, to fit the broadness of the Balmer line profiles well. The secondary would thus be more massive, and the primary less massive, and as such, including a mass ratio of approximately one, all evidence points towards WDJ181058.67+311940.94 being a super-Chandrasekhar mass double white dwarf.

The critical time at which the two stars reach closest approach can be calculated using<sup>39</sup>

$$T_c(a_0) = \frac{5}{256} \frac{a_0^4 c^5}{G^3 M_1 M_2 (M_1 + M_2)} \quad (1)$$

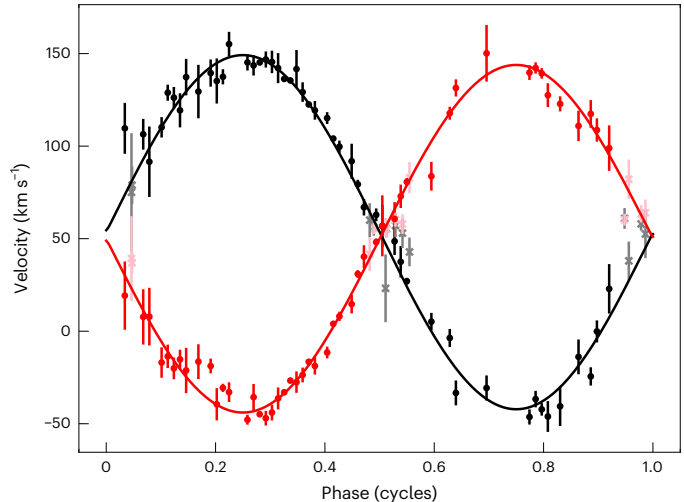


**Fig. 2 | The best-fit orbital solution phase-folded on the orbital period.** The hotter star (black) and the cooler star (red). The RV curves are plotted showing the velocity of the two stars across a full orbit, binned into 80 evenly spaced phase bins. In faded colours and with crossed markers are the RVs that were masked in searching for an orbital solution, which are also listed in Supplementary Table 1. One-sigma error bars are given as the standard deviation of 1,000 bootstrapping iterations.

where  $a_0$  is the semimajor axis of the binary at the present day and, for WDJ181058.67+311940.94,  $a_0 = 0.01601 \pm 0.00015$  A.U. This indicates that the stars will come into contact in  $22.6 \pm 1.0$  Gyr, whereas the less massive component will begin Roche lobe overflow and initiate mass transfer approximately 100 yr before the demise of binary.

### Modelling the fate of the binary system

To understand the fate of the binary system, we simulated its interaction when it was just about to merge using the star masses obtained through spectral fits to the VLT/UVES data. Videos of this simulation are presented in the Supplementary Information (Supplementary Videos 1 and 2). The spectral fits indicate that carbon–oxygen cores are appropriate for both white dwarfs, so we consider it highly unlikely that an accretion induced collapse will occur. This would require the more massive white dwarf to have a mass higher than  $1.2 M_{\odot}$  with an

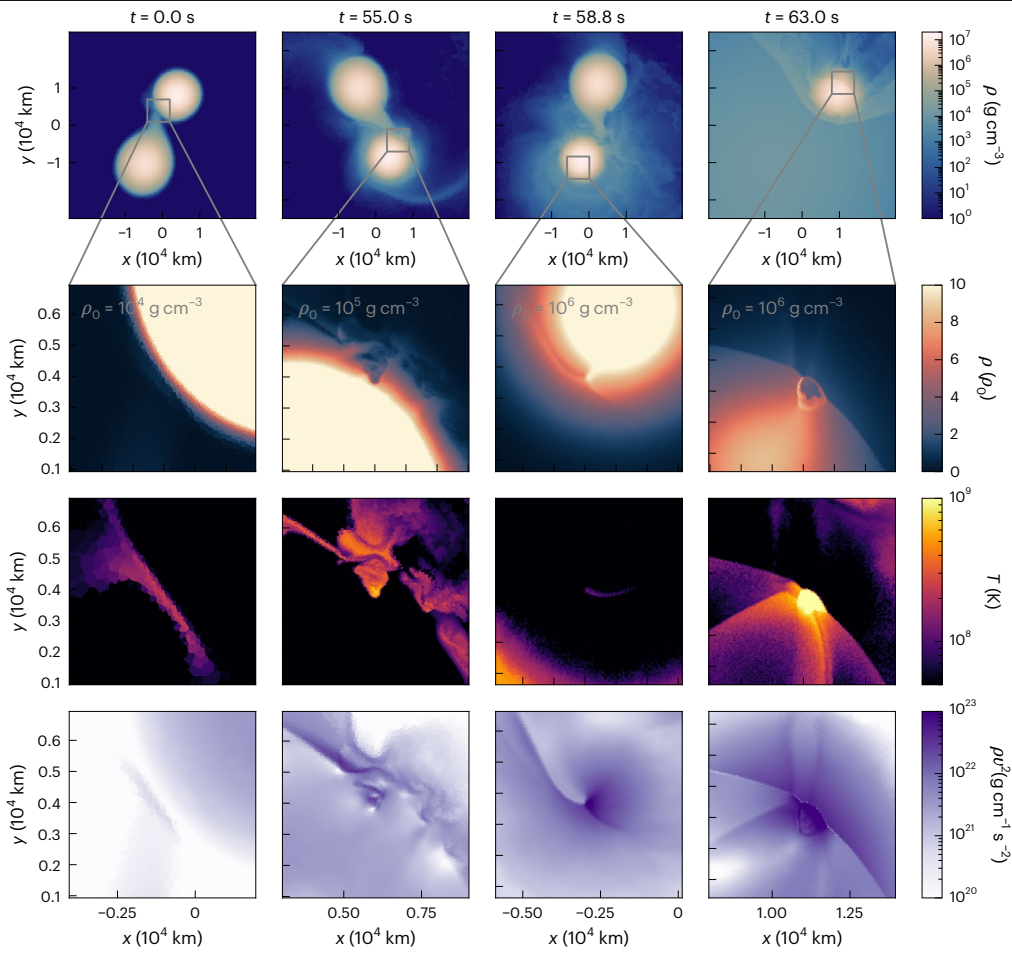


**Fig. 3 | Time evolution in slices of the binary systems close to merger.** The first column shows the time when we stop the accelerated inspiral and continue to evolve the binary system self-consistently. The second and third columns show the time when the helium detonation ignites on the surface of the primary white dwarf, and the time when the shock wave that is driven into the core of the primary by the helium detonation converges in a single point. The fourth column

shows the same shock convergence in the core of the secondary white dwarf. The top row shows slices of density in the plane of rotation and the three below are zoomed insets at the point of interest. Top to bottom, density, temperature and kinetic energy density. The shock convergence points in both white dwarfs occur at densities high enough to be very likely to ignite a carbon detonation and destroy the white dwarf.

oxygen–neon core to avoid dynamical ignition before or during the merger. We used the moving-mesh code AREPO<sup>40–42</sup> in a similar set-up to previous work<sup>43</sup>. The stars were given realistic composition profiles and placed in corotation before applying an accelerated inspiral term that removed angular momentum in the same way as gravitational waves. We switched on a live nuclear reaction network with 55 isotopes<sup>43,44</sup> at an orbital period of 39 s as the temperature of the accretion stream at the impact spot approached that required for a thermonuclear runaway. We show an overview of the dynamic evolution of the binary system in Fig. 3. The interaction of the accretion stream with the surface of the primary white dwarf ignites a helium detonation close to the point of interaction (second column of Fig. 3). The helium detonation then wraps around the primary white dwarf and sends a shock wave into its core that converges at a single point. This ignites a second detonation that completely destroys the primary white dwarf. When the shock wave of its explosion hits the secondary white dwarf, the double detonation mechanism repeats itself. The shock wave from the detonation of the primary ignites a helium detonation near the surface of the secondary which drives a shock wave into its core. It is sufficient to ignite the core detonation, destroying the secondary white dwarf as well.

There is no bound remnant and the ejecta of the explosion contain the total mass of the initial binary, having a total explosion energy of  $1.2 \times 10^{51}$  erg. We show the structure and composition of the ejecta in Fig. 4. The outermost layers of ejecta are the ashes of the helium

detonation of the primary white dwarf. They consist mostly of intermediate mass elements, dominated by silicon, sulfur and argon. Below them sit the ashes of the carbon–oxygen core of the primary white dwarf. Again they consist mostly of intermediate mass elements, but also contain  $0.13 M_\odot$  of iron group elements, in particular,  $0.10 M_\odot$  of radioactive  $^{56}\text{Ni}$  that will power the light curve. The resulting supernova has a maximum brightness in the B band of  $M_B = -16.4$  ( $m_B = -14.7$ ) and a maximum brightness in the V band of  $M_V = -17.8$  ( $m_V = -16.1$ ), and is most likely to appear as a subluminous type Ia supernova.

#### Galactic rates of super-Chandrasekhar mass double white dwarfs

We can use WDJ181058.67+311940.94 to observationally predict the number of super-Chandrasekhar mass double white dwarfs in the Milky Way. We start by assuming that WDJ181058.67+311940.94 and NLTT 12758 are the only two within 49 pc and make the rudimentary assumption that double white dwarfs are evenly scattered around the Milky Way having a cylindrical disk with radius  $R_{\max} = 15$  kpc and scale height  $h_z = 300$  pc. The white dwarf birth rate is estimated to be approximately  $1.4 \times 10^{-12} \text{ pc}^{-3} \text{ yr}^{-1}$  (ref. 45). There are 1,076 white dwarfs within the volume-complete 40 pc Gaia sample<sup>16</sup> and extrapolated to 49 pc we would have 1,978 white dwarfs. This means that the birth rate of super-Chandrasekhar mass double white dwarfs in the Galaxy becomes greater than approximately  $6.0 \times 10^{-4} \text{ yr}^{-1}$ .

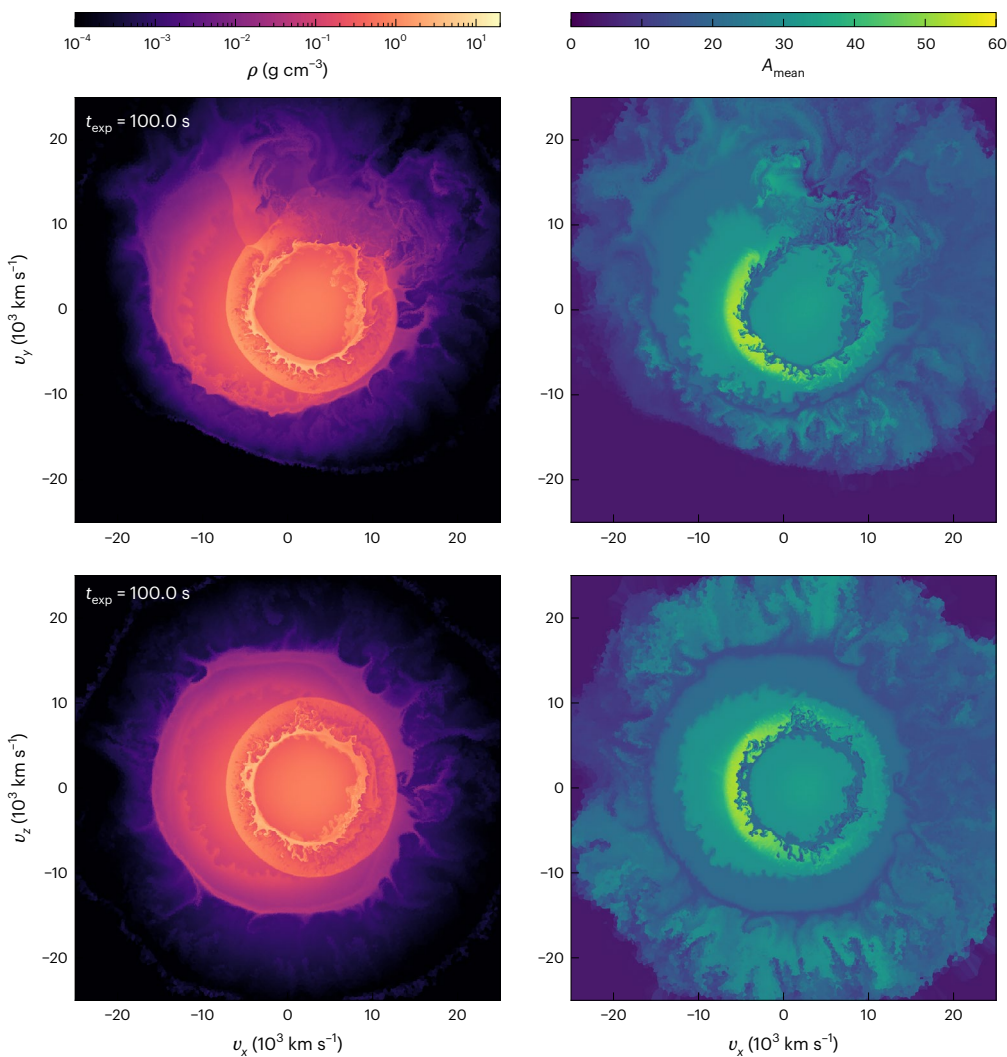


**Fig. 4 | Ejecta profiles after the explosion of both stars.** Slices of density (left column) and mean atomic weight (right column) of the supernova ejecta in homologous expansion for a time ( $t_{\text{exp}}$ ) 100 s after ignition of the first helium detonation. The top row shows slices in the original plane of rotation and the bottom row shows slices perpendicular to it. The outer layers are close

to spherically symmetrical, although significant deviations from spherical symmetry exist in the plane of rotation. The iron group elements (including  $^{56}\text{Ni}$ ) are essentially all produced in the explosion of the primary white dwarf and form a half-sphere around the ejecta of the secondary white dwarf.

Moreover, we can also calculate an observed rate of type Ia supernovae arising from super-Chandrasekhar mass double white dwarfs using WD181058.67+311940.94 ( $T_c = 22.6 \pm 1.0$  Gyr) and NLTT 12758 ( $T_c = 139 \pm 9$  Gyr). The frequency of the two events combined imply a supernova rate of about once every 19 Gyr within 49 pc or  $(1.04 \pm 0.04) \times 10^{-16}$  yr $^{-1}$  pc $^{-3}$ . When fully extrapolated with the cylindrical disk approximation, the observed rate of type Ia supernovae from super-Chandrasekhar mass double white dwarfs in the Milky Way hence becomes at least  $(4.4 \pm 0.2) \times 10^{-5}$  yr $^{-1}$ , although the quoted uncertainty does not account for uncertainties on the Galactic model. This result serves as a minimum based on the 49 pc population as it remains possible that other systems exist within the same radius.

Evidently, the magnitude of super-Chandrasekhar mass systems approaches the  $(2.8 \pm 0.6) \times 10^{-3}$  yr $^{-1}$  rate predicted for all evolutionary channels leading to a type Ia (refs. 4, 33, 34), but we must recall that these two systems are set to come together in more than a Hubble time and consider that the present observed supernova rate from these systems is about sixty times smaller. As such, the rates from Milky Way progenitors through the hot subdwarf binary channel and the double white dwarf channel are about the same, together accounting for about 3% of the Galactic rate. Synthetic populations suspect that around 60% of

the Galactic birth rate of type Ia progenitors comes from the double degenerate channel<sup>46,47</sup>, as is the case for WD181058.67+311940.94. The large missing fraction is especially mysterious given the high completion rate of the 40 pc sample of white dwarfs<sup>16</sup>. Contribution to the double white dwarf type Ia rate from sub-Chandrasekhar mass limits detonation could at least be a partial solution to make up for the deficit, where a mass-period distribution of double white dwarfs in a volume/magnitude limited sample serves as a means to put this to the test<sup>26</sup>. To date, there have been no sub-Chandrasekhar mass type Ia progenitor candidates inside a 50 pc radius, so ongoing efforts are crucial to properly quantify the number of massive double white dwarf binaries in our local neighbourhood and the Milky Way.

## Conclusion

We have presented a compact, super-Chandrasekhar mass double white dwarf binary which will merge in close to a Hubble time, having an orbital period of 14.24 h. With a total mass of  $1.555 \pm 0.044 M_{\odot}$ , WD181058.67+311940.94 is the most massive double white dwarf binary confirmed to date. We predict it to explode as a quadruple detonation and be destroyed completely. With all the mass ejected and a total explosion energy of  $1.2 \times 10^{51}$  erg, but only  $0.1 M_{\odot}$  of  $^{56}\text{Ni}$  in the ejecta,

it will appear as a subluminous type Ia supernova with a peak apparent magnitude of approximately  $m_B = -14.7$  and  $m_V = -16.1$ .

The lack of observational evidence of compact and massive double white dwarf binaries has long troubled the theory that double white dwarfs are the dominating evolutionary channel of type Ia detonations<sup>3</sup>. WDJ181058.67+311940.94 provides tentative observational evidence that super-Chandrasekhar mass systems with short merger times do exist in the Milky Way, and when combined with the close proximity of 49 pc the rate of super-Chandrasekhar mass double white dwarfs born in the Milky Way is at least  $6.0 \times 10^{-4} \text{ yr}^{-1}$ . This draws closer the disparity between the observed and predicted birth rates of super-Chandrasekhar mass systems, although the observed rate is still approximately two times smaller. However, there remains a large deficit in the rate of type Ia supernovae from the progenitor systems. A small fraction of the Milky Way rate is accounted for, now with an equal contribution from double white dwarf and white dwarf+hot subdwarf binaries.

Being discovered through a medium-resolution search of over-luminous double white dwarfs<sup>26</sup>, which up to a magnitude limit of  $G < 17$  mag is approximately 20% complete, it is entirely plausible that more super-Chandrasekhar mass double white dwarfs reside in our Galactic neighbourhood and that we have the spectroscopic ability to resolve the formation channel of type Ia supernovae. Deeper completeness through photometric and spectroscopic surveys in the coming years, as well the inauguration of space-based gravitational wave detectors in the next decade, will be pivotal in detecting ultracompact binaries on the cusp of detonation<sup>48,49</sup>. Combined efforts surveying type Ia progenitors across the full range of orbital periods will be the ultimate means to accurately quantify the contribution of double white dwarfs to type Ia supernovae.

## Methods

### Observations

WDJ181058.67+311940.94 was first discovered as part of the DBL survey<sup>26</sup> using medium-resolution spectra ( $R = 8,800$ ) on the 4.2 m WHT with the ISIS. Two other ISIS exposures were taken on the nights 13 and 14 April 2019 using the R600B and R1200R gratings with a 1.2' slit resulting in a spectral resolution of  $R = 3,000$  at H $\alpha$  and these spectra are included in the full orbital analysis of the double white dwarf. The blue and red set-ups had a wavelength calibration accuracy of approximately 3 km s $^{-1}$  and 2 km s $^{-1}$ , respectively.

We conducted a continued observational campaign to derive phase-resolved RVs of the double white dwarf binary. We utilized the 2.5 m Isaac Newton Telescope (INT) with the IDS over the nights 4–7 September 2019 (11 exposures, 1,800 s each) and 24 September 2019 (4 exposures, 900 s each) with the Red+2 detector and a 1.2' slit width, resulting in a spectral resolution of  $R = 6,300$ . Further phase-resolved spectra were taken with the INT on the nights 25 and 26 August 2024 with the H1800V grating at a resolution of  $R = 9,400$  (20 exposures, 1,500 s each). An arc lamp exposure was taken every 45 min of observing time and the science images were wavelength calibrated by interpolation of the nearest two arcs. The wavelength calibration accuracy per frame was approximately 2 km s $^{-1}$ .

Bias, flat field and spectrophotometric flux standard star images were taken on all nights and applied in the reduction. All data from the WHT and the INT were reduced using the MOLLY suite<sup>50</sup> using an optimal extraction algorithm<sup>51</sup>.

These data were supplemented with 18 exposures of length 1,500 s on the 2.56 m NOT using the FIES in low-resolution mode ( $R = 25,000$ ), having a wavelength calibration accuracy of approximately  $\pm 150 \text{ m s}^{-1}$ . Observations were obtained through a staff queue at random times, typically being two consecutive exposures, and through a NOT fast-track proposal. All FIES data were reduced using its automated data reduction pipeline, FIEStool<sup>52</sup>. We also obtained five exposures with the NOT ALFOSC with a 0.5" slit width, producing spectra at  $R = 10,000$

with wavelength range 6,330–6,870 Å on 1 and 2 June 2024. The data were reduced with the PYPEIT Python package<sup>53</sup>.

A continuous observing window of 4.5 h was obtained through directors discretionary time on the 8.2 m VLT with the UVES. Each exposure lasted for 730 s with a readout time between exposures of 45 s, totalling 20 exposures. We employed an observing set-up of the dichroic 1 mode with central wavelengths of 3,900 Å and 5,640 Å for the blue and red arms, giving a wavelength range that covered the full visible spectrum apart from gaps of 80 Å at 4,580 Å and 5,640 Å. A slit width of 1.0" and a 2  $\times$  2 binning granted a spectral resolution  $R = 20,000$  and the wavelength calibration accuracy was approximately 200 m s $^{-1}$  (refs. 54,55).

In deriving final RV errors for these data (Supplementary Table 1), the wavelength calibration error was added in quadrature to the statistical error.

### Atmospheric fitting of optical data

We used the package WD-BASS<sup>56</sup> to fit atmospheric parameters to the spectra from VLT/UVES. For synthetic spectra, we utilized the 3D-NLTE model grid introduced in ref. 26, which was constructed using the 3D-LTE models of ref. 57 with a further NLTE correction factor applied using the NLTE and LTE synthetic spectra described in ref. 58. The two stars were scaled using temperature–log  $g$ –radius relationships with the evolutionary track models of ref. 59 when  $M \leq 0.393 M_\odot$ , of ref. 60 when  $0.393 < M < 0.45 M_\odot$ , and the hydrogen-rich envelope evolutionary sequences of ref. 61 otherwise. These boundaries come from the expectation that a white dwarf with a mass below  $0.45 M_\odot$  has a helium core and those larger have a carbon–oxygen core. The model spectra were converted from an Eddington flux to that observed at Earth and reddened with an extinction coefficient  $A(V) = 0.0312 \text{ mag}$  (ref. 62) and colour excess  $E(B-V) = A(V)/3.1$  using the reddening curves of ref. 63.

We applied an atmospheric fitting technique that is very similar to that described in ref. 26 by linearly normalizing and fitting the Balmer spectral lines of the UVES data using a Markov Chain Monte Carlo algorithm, maximizing the likelihood for a best-fit solution. We also utilized Pan-STARRS photometry<sup>64</sup> to perform a hybrid fit using both datasets simultaneously. With high signal-to-noise ratio data, we were able to fit all Balmer lines from H $\alpha$  to H11. Furthermore, to give the photometric and spectroscopic data a similar weight, we applied an extra weighting ( $\times 1,000$ ) to the photometric fit. Without this weighting, the spectra would have overdominated the best-fit solution. Only spectra taken at the times where a distinct double-line splitting was evident at H $\alpha$  were modelled to avoid fitting degeneracies between the two stars, of which there were 10 each (a total of 20). In deriving errors, we individually fitted each red-arm spectrum that revealed a double-lined H $\alpha$  split along with the nearest-in-time blue-arm spectrum while weighting the photometry by  $\times 100$ . Then we took the standard deviation of all measurements to be the error in the star's surface gravity and temperature. The new best-fit atmospheric parameters are stated in Table 1, which are entirely consistent with previous values<sup>26</sup>.

### Atmospheric fitting of ultraviolet data

We performed an independent spectroscopic fit using a previously published HST spectrum<sup>38</sup>. WDJ181058.67+311940.94 was observed for a single 1,000 s exposure using the COS on 19 February 2022. The observation had a central wavelength of 1,291 Å with the G130M grating, giving a resolution of  $R = 12,000$ –16,000 and a wavelength range of 1,130–1,430 Å with a gap at 1,278–1,288 Å due to the positioning of the two detector segments. Given the vastly different methods and the fact that WDJ181058.67+311940.94 is not double lined at Lyman- $\alpha$  in the ultraviolet data, no RVs were extracted, but the predicted RVs of the two stars at the centre of exposure ( $-37.8 \text{ km s}^{-1}$  for the more massive and  $139.6 \text{ km s}^{-1}$  for the less massive star, respectively) were fixed in the fitting procedure.

Our spectral fitting method was identical to that presented in ref. 38 with the only exceptions being that a second hydrogen-rich atmosphere white dwarf is included in the model, in which we adopt  $A(V) = 0.0312$  mag and in which the mid-exposure RV of the two stars is considered. A hybrid (spectroscopic and photometric) fit was performed with no extra error weighting applied using the HST/COS spectrum and photometry from Pan-STARRS g, r, i, z, y (ref. 64), fixing the distance to Gaia DR3 parallax. Updated model atmospheres<sup>65</sup> with a white dwarf mass–radius relationship<sup>61</sup> were used to fit the absolute fluxes. In addition, strong absorption lines affecting the continuum were masked in the COS spectrum<sup>38</sup>. To address the inconsistencies reported between ultraviolet and optical parameters<sup>38</sup>, a systematic offset of 1% in  $T_{\text{eff}}$  and 0.1 dex in  $\log g$  were added to the ultraviolet values of both stars in the hybrid fitting, whereas trial values in the optical were unchanged. The best-fit model to the spectra are shown in Fig. 1, and the results of our atmospheric fitting are given in Table 1 and compared with the optical solution. We found a total mass of  $1.537 \pm 0.018 M_{\odot}$  through this analysis, which again is consistent with previous values<sup>26</sup>.

To provide a final adopted value from the atmospheric fitting inclusive of the results from the optical and the ultraviolet datasets, we concatenated the distributions obtained for each parameter to then quote the median and 68% confidence interval on the  $T_{\text{eff}}$  and  $\log g$  and interpolated these parameters to obtain masses. The adopted values are quoted in Tables 1 and 2.

### RVs and orbital parameters

WD-BASS<sup>36</sup> was again used to obtain RVs for all of the optical spectra. The best-fit synthetic spectrum agrees with the data extremely well (Fig. 1), but even with the correction of NLTE effects to the model gridline cores, the synthetic model flux is overpredicted in the line cores of H $\alpha$ . To obtain the most accurate template for RV extraction possible, we fitted a Gaussian model to the H $\alpha$  line cores of both stars combined with a four-term polynomial to model the broader wings of H $\alpha$ , all within 10 Å of the H $\alpha$  centre. The centre of a H $\alpha$  absorption was isolated as the splitting of the two stars is most apparent around the non-thermal equilibrium line cores and hence the stars are most easily disentanglable. This method best modelled the shape of the spectral area around the line cores for the high signal-to-noise ratio and high resolution UVES spectra, but not for all other data sources. Instead, we took the result of the best-fit synthetic spectrum and added an extra Gaussian component at the line cores of H $\alpha$  for both stars (following the method described in Section 4.4 of ref. 26), which improved the line-core shape significantly. The Gaussians were fitted to all relevant spectra simultaneously and this final template spectrum was then used for RV extraction in WD-BASS. We started by fitting the RV of both stars to each spectrum by taking the median of 1,000 bootstrapping iterations and taking errors as the standard deviation of this bootstrapped posterior distribution.

With the full set of 82 RV measurements (Supplementary Table 1), we then searched for an orbital period,  $P$ , by minimizing the  $\chi^2$  of equation (2) for trial semi-amplitudes ( $K_1, K_2$ ) and velocity offsets ( $\gamma_1, \gamma_2$ ) of each star using a least squares algorithm, where

$$PK_{1,2}^3 = \frac{2\pi GM_{2,1}^3 \sin(i)^3}{(M_{1,2} + M_{2,1})^2} \quad (2)$$

Upper bounds on the semi-amplitudes  $K_{\text{max},1}$  and  $K_{\text{max},2}$  were set for a trial period by applying an edge-on ( $i = 90^\circ$ ) inclination for a  $1.4 M_{\odot} + 0.15 M_{\odot}$  double white dwarf in a Keplerian orbit (the maximum and observed minimum mass of a white dwarf, respectively). There is no indication of eccentricity from the RVs, so the orbit was assumed to be circularized ( $e = 0$ ). In the process, we noticed a deviation from Keplerian motion around conjunction which is caused by degeneracy in the fitted RVs as the stars spectrally overlap. This is unsurprising as the velocity resolution of the ALFOSC, ISIS and IDS data was around 30–40 km s $^{-1}$ , whereas

in the higher resolution FIES spectra a lower signal-to-noise ratio led to the same degeneracies. We decided to ignore these RVs when fitting the orbital motion by masking measurements that were within 15 km s $^{-1}$  of the RV of each star at conjunction. All RVs from the UVES spectra within this range were utilized as its high signal-to-noise combined with twice the velocity resolution did not cause any noticeable deviation. With the final periodogram, two prominent peaks appeared at very similar solutions; we adopted the solution with a 14.2356 h period and another at 14.2308 h, but the second one could be rejected owing to a gravitational redshift difference that would be a strong outlier from that expected in the atmospheric solution.

Returning to equation (2) with the final orbital solution and taking into account all combinations of masses from the atmospheric analysis, we conclude that WDJ181058.67+311940.94 has an inclination  $i \approx 35\text{--}45$  deg. We analysed the TESS<sup>66</sup> light curve of WDJ181058.67+311940.94 in all cadences to search for any photometric signature of photometric variability with Lomb–Scargle<sup>67,68</sup> and boxed-least-squares periodograms but found no variation on the orbital period. For an eclipse to be witnessed in this system, the inclination would have to be above 89.64 deg and photometric variability from ellipsoidal modulation or irradiation is minute for a system with 14.24 h orbital period. The Doppler beaming from the two stars is nullified by their opposing motion of near-identical RV amplitudes and a similar flux contribution<sup>69</sup>, and hence non-eclipsing forms of variability are not expected.

### Modelling the fate of the binary system

We created two white dwarfs from the premain sequence phase using the stellar evolution code MESA<sup>70–75</sup>, evolving them to carbon–oxygen white dwarfs of  $0.87 M_{\odot}$  and  $0.71 M_{\odot}$ . These masses align with observations from VLT/UVES spectra fitting. Compared with previous merger simulations, using self-consistent models evolved in MESA allowed us to start from realistic composition profiles. In particular, the two white dwarfs have a helium shell of  $8 \times 10^{-3} M_{\odot}$  (for the  $0.71 M_{\odot}$  white dwarf) and  $3 \times 10^{-3} M_{\odot}$  (for the  $0.87 M_{\odot}$  white dwarf).

We then created two three-dimensional white dwarfs in hydrostatic equilibrium with the same masses and abundance profiles in AREPO. We resolved the white dwarfs with cells with a roughly constant mass of  $10^{-7} M_{\odot}$  and used a passive scalar to resolve the helium shells of both white dwarfs even better with a mass resolution of  $10^{-8} M_{\odot}$ . We relaxed both white dwarfs in isolation for ten dynamical timescales, actively dampening any gas velocities for the first half of this time. The density and composition profiles of the relaxed white dwarfs, in particular close to the surface, well resembled the initial one-dimensional profiles obtained from MESA.

We put both white dwarfs into a binary system in corotation with an initial period of 73 s. At this period, the separation is about 1.5 times larger than the separation where the secondary white dwarf will fill its Roche lobe. We applied an accelerated inspiral term that removes angular momentum in the same way as gravitational waves, but on a much faster timescale. In this way, we obtained a binary system in equilibrium when mass transfer started on a scale that we could resolve in the simulation. At this time, the physical system would have transferred mass at a low rate for possibly hundreds of years, but the total mass transferred is likely to be negligible. The secondary white dwarf eventually started filling and then overfilling its Roche lobe, and we stopped the accelerated inspiral when the density at the inner Lagrange point between the white dwarfs reached  $2 \times 10^4 \text{ g cm}^{-3}$ . Only then did the density in the accretion stream become large enough to dynamically affect the surface of the primary white dwarf<sup>43,76,77</sup>.

The binary system had now shrunk to a separation of  $0.03 R_{\odot}$  and an orbital period of 39 s. We then continued to evolve the binary system conservatively and switched on a live nuclear reaction network with 55 isotopes<sup>43,44</sup>. After evolving the binary system conservatively for 55 s, the interaction of the accretion stream with the surface of the primary

white dwarf ignited a helium detonation close to the point of interaction (second column of Fig. 3), which is consistent with previous simulations of more massive white dwarf binaries<sup>77–79</sup>. As in the classic double detonation scenario where the helium detonation is caused by instabilities in a massive helium shell<sup>80,81</sup>, the helium detonation wraps around the primary white dwarf. It sends a shock wave into the core of the white dwarf, that converges in a single point at a density of  $9.6 \times 10^6 \text{ g cm}^{-3}$ . Because of a lack of numerical resolution, the simulation does not self-consistently ignite a carbon detonation there, but resolved ignition simulations indicated that, at this density, we expect a detonation to form at the convergence point<sup>82,83</sup>. To model the ignition of the detonation when the shock converges in the simulation, we set the temperature of 178 cells that contained  $1.8 \times 10^{-5} M_\odot$  around the convergence point to  $5 \times 10^9 \text{ K}$ . This injected  $4.8 \times 10^{46} \text{ erg}$  (which is negligible compared with the energy release of the whole simulation) and ignited the detonation. The detonation completely destroyed the primary white dwarf. When the shock wave of its explosion hit the secondary white dwarf, the double detonation mechanism repeated itself. The shock wave ignited a helium detonation that drove a shock wave into the core and converged at a density of  $8.5 \times 10^6 \text{ g cm}^{-3}$ . In this case, carbon burning started at the convergence point, but not strongly enough to start a detonation. We again ignited a detonation at the convergence point by setting the temperature of 708 cells that contained  $6.9 \times 10^{-5} M_\odot$  to  $6 \times 10^9 \text{ K}$ , which injected  $8.2 \times 10^{47} \text{ erg}$  and was sufficient to ignite the detonation that then destroyed the secondary white dwarf as well.

The total explosion energy was  $1.2 \times 10^{51} \text{ erg}$ . The core of the secondary white dwarf ignited 4.2 s after the core of the primary white dwarf. At this time, the ashes of the primary white dwarf had already expanded far beyond the secondary white dwarf. So when the latter exploded as well, its ejecta expanded into and remained in the centre of the ejecta of the primary white dwarf<sup>43</sup>. The outermost layers of ejecta were the ashes of the helium detonation of the primary white dwarf. The centre of the ejecta consisted of the ashes of the secondary white dwarf, which contained  $0.25 M_\odot$  of oxygen,  $0.4 M_\odot$  of intermediate mass elements and only  $0.01 M_\odot$  of iron group elements, with a roughly equal fraction of  $^{56}\text{Ni}$  and  $^{54}\text{Fe}$ .

We obtained preliminary synthetic light curves from spherically averaging the ejecta and computing light curves with the Monte Carlo radiation transport code ARTIS<sup>84,85</sup>. The resulting supernova had a maximum brightness in the B band of  $M_B = -16.4$  ( $m_B = -14.7$ ) and a maximum brightness in the V band of  $M_V = -17.8$  ( $m_V = -16.1$ ), which is consistent with traditional double detonation models of single white dwarfs with a similar mass to our primary white dwarf, because the secondary white dwarf does not produce any significant amount of radioactive  $^{56}\text{Ni}$  (refs. 86–88). That said, our explosion is likely to have avoided the imprint of thick helium shells on light curves and spectra<sup>88–90</sup>. It most likely appeared as a subluminous type Ia supernova. However, the obvious large-scale asymmetries visible in Fig. 4 indicate that three-dimensional synthetic observables will be needed to make any reliable statement about the expected display of this supernova<sup>79,88</sup>. These will be presented and discussed as part of a larger sample of merger simulations in the future. This new simulation also supports previous work which suggests that both stars will explode in massive double white dwarf binaries that are about to merge<sup>43,91,92</sup>.

## Data availability

All spectra and photometric survey measurements are available through the respective data archives, which are publicly available, or upon request to the authors. The observed RVs are published in Supplementary Table 1.

## Code availability

The fitting package WD-BASS that was used to determine atmospheric parameters and radial velocities is available at <https://github.com/JamesMunday98/WD-BASS>.

## References

1. Nugent, P. E. et al. Supernova SN 2011fe from an exploding carbon-oxygen white dwarf star. *Nature* **480**, 344–347 (2011).
2. Bloom, J. S. et al. A compact degenerate primary-star progenitor of SN 2011fe. *Astrophys. J. Lett.* **744**, L17 (2012).
3. Maoz, D. & Mannucci, F. Type-Ia supernova rates and the progenitor problem: a review. *Publ. Astron. Soc. Aust.* **29**, 447–465 (2012).
4. Liu, Z.-W., Röpke, F. K. & Han, Z. Type Ia supernova explosions in binary systems: a review. *Res. Astron. Astrophys.* **23**, 082001 (2023).
5. Soker, N. Supernovae in 2023 (review): possible breakthroughs by late observations. *Open J. Astrophys.* **7**, 31 (2024).
6. Webbink, R. F. Double white dwarfs as progenitors of R Coronae Borealis stars and type I supernovae. *Astrophys. J.* **277**, 355–360 (1984).
7. Iben Jr, I. & Tutukov, A. V. Supernovae of type I as end products of the evolution of binaries with components of moderate initial mass. *Astrophys. J. Suppl. Ser.* **54**, 335–372 (1984).
8. Nelemans, G., Yungelson, L. R., Portegies Zwart, S. F. & Verbunt, F. Population synthesis for double white dwarfs. I. Close detached systems. *Astron. Astrophys.* **365**, 491–507 (2001).
9. Postnov, K. A. & Yungelson, L. R. The evolution of compact binary star systems. *Living Rev. Relativ.* **17**, 3 (2014).
10. Ruiter, A. J. et al. Delay times and rates for Type Ia supernovae and thermonuclear explosions from double-detonation sub-Chandrasekhar mass models. *Mon. Not. R. Astron. Soc.* **417**, 408–419 (2011).
11. Burdge, K. B. et al. A systematic search of Zwicky transient facility data for ultracompact binary LISA-detectable gravitational-wave sources. *Astrophys. J.* **905**, 32 (2020).
12. Brown, W. R. et al. The ELM survey. VIII. Ninety-eight double white dwarf binaries. *Astrophys. J.* **889**, 49 (2020).
13. Ren, L. et al. A systematic search for short-period close white dwarf binary candidates based on Gaia EDR3 catalog and Zwicky Transient Facility data. *Astrophys. J. Suppl. Ser.* **264**, 39 (2023).
14. Toonen, S., Hollands, M., Gänsicke, B. T. & Boekholt, T. The binarity of the local white dwarf population. *Astron. Astrophys.* **602**, A16 (2017).
15. Hollands, M. A., Tremblay, P. E., Gänsicke, B. T., Gentile-Fusillo, N. P. & Toonen, S. The Gaia 20 pc white dwarf sample. *Mon. Not. R. Astron. Soc.* **480**, 3942–3961 (2018).
16. O'Brien, M. W. et al. The 40 pc sample of white dwarfs from Gaia. *Mon. Not. R. Astron. Soc.* **527**, 8687–8705 (2024).
17. Toonen, S., Nelemans, G. & Portegies Zwart, S. Supernova Type Ia progenitors from merging double white dwarfs. Using a new population synthesis model. *Astron. Astrophys.* **546**, A70 (2012).
18. Rebassa-Mansergas, A., Toonen, S., Korol, V. & Torres, S. Where are the double-degenerate progenitors of Type Ia supernovae? *Mon. Not. R. Astron. Soc.* **482**, 3656–3668 (2019).
19. Li, Z., Chen, X., Ge, H., Chen, H.-L. & Han, Z. Influence of a mass transfer stability criterion on double white dwarf populations. *Astron. Astrophys.* **669**, A82 (2023).
20. Kawka, A. et al. A fast spinning magnetic white dwarf in the double degenerate, super-Chandrasekhar system NLTT 12758. *Mon. Not. R. Astron. Soc.* **466**, 1127–1139 (2017).
21. Maxted, P. F. L., Marsh, T. R. & Moran, C. K. J. The mass ratio distribution of short-period double degenerate stars. *Mon. Not. R. Astron. Soc.* **332**, 745–753 (2002).
22. Karl, C. A. et al. Binaries discovered by the SPY project. III. HE 2209-1444: a massive, short period double degenerate. *Astron. Astrophys.* **410**, 663–669 (2003).
23. Nelemans, G. et al. Binaries discovered by the SPY project. IV. Five single-lined DA double white dwarfs. *Astron. Astrophys.* **440**, 1087–1095 (2005).

24. Rebassa-Mansergas, A. et al. Orbital periods and component masses of three double white dwarfs. *Mon. Not. R. Astron. Soc.* **466**, 1575–1581 (2017).

25. Munday, J. et al. Two decades of optical timing of the shortest-period binary star system HM Cancri. *Mon. Not. R. Astron. Soc.* **518**, 5123–5139 (2023).

26. Munday, J. et al. The DBL Survey I: discovery of 34 double-lined double white dwarf binaries. *Mon. Not. R. Astron. Soc.* **532**, 2534–2556 (2024).

27. Pelisoli, I. et al. A hot subdwarf-white dwarf super-Chandrasekhar candidate supernova la progenitor. *Nat. Astron.* **5**, 1052–1061 (2021).

28. Luo, C. et al. A born ultramassive white dwarf-hot subdwarf super-Chandrasekhar candidate. Preprint at <https://arxiv.org/abs/2404.04835> (2024).

29. Maxted, P. F. L., Marsh, T. R. & North, R. C. KPD 1930+2752: a candidate Type Ia supernova progenitor. *Mon. Not. R. Astron. Soc.* **317**, L41–L44 (2000).

30. Geier, S. et al. The hot subdwarf B + white dwarf binary KPD 1930+2752. A supernova type Ia progenitor candidate. *Astron. Astrophys.* **464**, 299–307 (2007).

31. Pelisoli, I., Vos, J., Geier, S., Schaffenroth, V. & Baran, A. S. Alone but not lonely: observational evidence that binary interaction is always required to form hot subdwarf stars. *Astron. Astrophys.* **642**, A180 (2020).

32. Dawson, H. et al. A 500 pc volume-limited sample of hot subluminous stars. I. Space density, scale height, and population properties. *Astron. Astrophys.* **686**, A25 (2024).

33. Li, W. et al. Nearby supernova rates from the Lick Observatory Supernova Search. III. The rate-size relation, and the rates as a function of galaxy Hubble type and colour. *Mon. Not. R. Astron. Soc.* **412**, 1473–1507 (2011).

34. Maoz, D., Mannucci, F. & Nelemans, G. Observational clues to the progenitors of Type Ia supernovae. *Annu. Rev. Astron. Astrophys.* **52**, 107–170 (2014).

35. Pan, T., Kasen, D. & Loeb, A. Pair-instability supernovae at the epoch of reionization. *Mon. Not. R. Astron. Soc.* **422**, 2701–2711 (2012).

36. Lacchin, E., Calura, F. & Vesperini, E. On the role of Type Ia supernovae in the second-generation star formation in globular clusters. *Mon. Not. R. Astron. Soc.* **506**, 5951–5968 (2021).

37. Jiménez, N., Tissera, P. B. & Matteucci, F. Type Ia supernova progenitors and chemical enrichment in hydrodynamical simulations. I. The single-degenerate scenario. *Astrophys. J.* **810**, 137 (2015).

38. Sahu, S. et al. An HST COS ultraviolet spectroscopic survey of 311 DA white dwarfs. I. Fundamental parameters and comparative studies. *Mon. Not. R. Astron. Soc.* **526**, 5800–5823 (2023).

39. Peters, P. C. Gravitational radiation and the motion of two point masses. *Phys. Rev.* **136**, 1224–1232 (1964).

40. Springel, V. E pur si muove: Galilean-invariant cosmological hydrodynamical simulations on a moving mesh. *Mon. Not. R. Astron. Soc.* **401**, 791–851 (2010).

41. Pakmor, R. et al. Improving the convergence properties of the moving-mesh code AREPO. *Mon. Not. R. Astron. Soc.* **455**, 1134–1143 (2016).

42. Weinberger, R., Springel, V. & Pakmor, R. The AREPO public code release. *Astrophys. J. Suppl. Ser.* **248**, 32 (2020).

43. Pakmor, R. et al. On the fate of the secondary white dwarf in double-degenerate double-detonation Type Ia supernovae. *Mon. Not. R. Astron. Soc.* **517**, 5260–5271 (2022).

44. Pakmor, R., Edelmann, P., Röpke, F. K. & Hillebrandt, W. Stellar GADGET: a smoothed particle hydrodynamics code for stellar astrophysics and its application to Type Ia supernovae from white dwarf mergers. *Mon. Not. R. Astron. Soc.* **424**, 2222–2231 (2012).

45. Holberg, J. B., Oswalt, T. D., Sion, E. M. & McCook, G. P. The 25 parsec local white dwarf population. *Mon. Not. R. Astron. Soc.* **462**, 2295–2318 (2016).

46. Wang, B. et al. Birthrates and delay times of Type Ia supernovae. *Sci. China Phys. Mech. Astron.* **53**, 586–590 (2010).

47. Liu, D., Wang, B. & Han, Z. The double-degenerate model for the progenitors of Type Ia supernovae. *Mon. Not. R. Astron. Soc.* **473**, 5352–5361 (2018).

48. Korol, V. et al. Prospects for detection of detached double white dwarf binaries with Gaia, LSST and LISA. *Mon. Not. R. Astron. Soc.* **470**, 1894–1910 (2017).

49. Korol, V. et al. Expected insights on Type Ia supernovae from LISA's gravitational wave observations. *Astron. Astrophys.* **691**, A44 (2024).

50. Marsh, T. molly: 1D astronomical spectra analyzer. *Astrophysics Source Code Library* ascl:1907.012 (2019).

51. Marsh, T. R. The extraction of highly distorted spectra. *Publ. Astron. Soc. Pac.* **101**, 1032 (1989).

52. FIEStool. *Nordic Optical Telescope* <https://www.not.iac.es/instruments/fiestool/> (2024).

53. Prochaska, J. et al. Pypelt: the Python spectroscopic data reduction pipeline. *J. Open Source Softw.* **5**, 2308 (2020).

54. Whitmore, J. B., Murphy, M. T. & Griest, K. Wavelength calibration of the VLT-UVES spectrograph. *Astrophys. J.* **723**, 89–99 (2010).

55. Whitmore, J. B. & Murphy, M. T. Impact of instrumental systematic errors on fine-structure constant measurements with quasar spectra. *Mon. Not. R. Astron. Soc.* **447**, 446–462 (2015).

56. Munday, J. JamesMunday98/WD-BASS: v1.0.0. Zenodo <https://doi.org/10.5281/zenodo.11188044> (2024).

57. Tremblay, P. E. et al. 3D model atmospheres for extremely low-mass white dwarfs. *Astrophys. J.* **809**, 148 (2015).

58. Kilic, M., Bédard, A. & Bergeron, P. Hidden in plain sight: a double-lined white dwarf binary 26 pc away and a distant cousin. *Mon. Not. R. Astron. Soc.* **502**, 4972–4980 (2021).

59. Istrate, A. G. et al. Models of low-mass helium white dwarfs including gravitational settling, thermal and chemical diffusion, and rotational mixing. *Astron. Astrophys.* **595**, A35 (2016).

60. Althaus, L. G., Miller Bertolami, M. M. & Córscico, A. H. New evolutionary sequences for extremely low-mass white dwarfs. Homogeneous mass and age determinations and asteroseismic prospects. *Astron. Astrophys.* **557**, A19 (2013).

61. Bédard, A., Bergeron, P., Brassard, P. & Fontaine, G. On the spectral evolution of hot white dwarf stars. I. A detailed model atmosphere analysis of hot white dwarfs from SDSS DR12. *Astrophys. J.* **901**, 93 (2020).

62. Lallement, R., Vergely, J. L., Babusiaux, C. & Cox, N. L. J. Updated Gaia-2MASS 3D maps of Galactic interstellar dust. *Astron. Astrophys.* **661**, A147 (2022).

63. Gordon, K. D. et al. One relation for all wavelengths: the far-ultraviolet to mid-infrared Milky Way spectroscopic R(V)-dependent dust extinction relationship. *Astrophys. J.* **950**, 86 (2023).

64. Chambers, K. & Pan-STARRS Team. The Pan-STARRS1 Surveys. *Am. Astron. Soc. Meeting Abstracts* **231**, abstr. 102.01 (2018).

65. Koester, D. White dwarf spectra and atmosphere models. *Mem. Soc. Astron. Ital.* **81**, 921–931 (2010).

66. Ricker, G. R. et al. Transiting Exoplanet Survey Satellite (TESS). *J. Astron. Telesc. Instrum. Syst.* **1**, 014003 (2015).

67. Lomb, N. R. Least-squares frequency analysis of unequally spaced data. *Astrophys. Space Sci.* **39**, 447–462 (1976).

68. Scargle, J. D. Studies in astronomical time series analysis. II. Statistical aspects of spectral analysis of unevenly spaced data. *Astrophys. J.* **263**, 835–853 (1982).

69. Hermes, J. J. et al. Radius constraints from high-speed photometry of 20 low-mass white dwarf binaries. *Astrophys. J.* **792**, 39 (2014).

70. Paxton, B. et al. Modules for experiments in stellar astrophysics (MESA). *Astrophys. J. Suppl. Ser.* **192**, 3 (2011).

71. Paxton, B. et al. Modules for experiments in stellar astrophysics (MESA): planets, oscillations, rotation, and massive stars. *Astrophys. J. Suppl. Ser.* **208**, 4 (2013).

72. Paxton, B. et al. Modules for experiments in stellar astrophysics (MESA): binaries, pulsations, and explosions. *Astrophys. J. Suppl. Ser.* **220**, 15 (2015).

73. Paxton, B. et al. Modules for experiments in stellar astrophysics (MESA): convective boundaries, element diffusion, and massive star explosions. *Astrophys. J. Suppl. Ser.* **234**, 34 (2018).

74. Paxton, B. et al. Modules for experiments in stellar astrophysics (MESA): pulsating variable stars, rotation, convective boundaries, and energy conservation. *Astrophys. J. Suppl. Ser.* **243**, 10 (2019).

75. Jermyn, A. S. et al. Modules for experiments in stellar astrophysics (MESA): time-dependent convection, energy conservation, automatic differentiation, and infrastructure. *Astrophys. J. Suppl. Ser.* **265**, 15 (2023).

76. Guillochon, J., Dan, M., Ramirez-Ruiz, E. & Rosswog, S. Surface detonations in double degenerate binary systems triggered by accretion stream instabilities. *Astrophys. J. Lett.* **709**, L64–L69 (2010).

77. Pakmor, R., Kromer, M., Taubenberger, S. & Springel, V. Helium-ignited violent mergers as a unified model for normal and rapidly declining type Ia supernovae. *Astrophys. J. Lett.* **770**, L8 (2013).

78. Pakmor, R., Zenati, Y., Perets, H. B. & Toonen, S. Thermonuclear explosion of a massive hybrid HeCO white dwarf triggered by a He detonation on a companion. *Mon. Not. R. Astron. Soc.* **503**, 4734–4747 (2021).

79. Pakmor, R. et al. Type Ia supernova explosion models are inherently multidimensional. *Astron. Astrophys.* **686**, A227 (2024).

80. Livne, E. Successive detonations in accreting white dwarfs as an alternative mechanism for type Ia supernovae. *Astrophys. J. Lett.* **354**, L53 (1990).

81. Fink, M. et al. Double-detonation sub-Chandrasekhar supernovae: can minimum helium shell masses detonate the core? *Astron. Astrophys.* **514**, A53 (2010).

82. Seitenzahl, I. R., Meakin, C. A., Townsley, D. M., Lamb, D. Q. & Truran, J. W. Spontaneous initiation of detonations in white dwarf environments: determination of critical sizes. *Astrophys. J.* **696**, 515–527 (2009).

83. Shen, K. J. & Bildsten, L. The ignition of carbon detonations via converging shock waves in white dwarfs. *Astrophys. J.* **785**, 61 (2014).

84. Kromer, M. & Sim, S. A. Time-dependent three-dimensional spectrum synthesis for Type Ia supernovae. *Mon. Not. R. Astron. Soc.* **398**, 1809–1826 (2009).

85. Sim, S. A. Multidimensional simulations of radiative transfer in Type Ia supernovae. *Mon. Not. R. Astron. Soc.* **375**, 154–162 (2007).

86. Sim, S. A. et al. Detonations in sub-Chandrasekhar-mass C+O white dwarfs. *Astrophys. J. Lett.* **714**, L52–L57 (2010).

87. Shen, K. J., Boos, S. J., Townsley, D. M. & Kasen, D. Multidimensional radiative transfer calculations of double detonations of sub-Chandrasekhar-mass white dwarfs. *Astrophys. J.* **922**, 68 (2021).

88. Collins, C. E., Gronow, S., Sim, S. A. & Röpke, F. K. Double detonations: variations in Type Ia supernovae due to different core and He shell masses. II. Synthetic observables. *Mon. Not. R. Astron. Soc.* **517**, 5289–5302 (2022).

89. Kromer, M. et al. Double-detonation sub-Chandrasekhar supernovae: synthetic observables for minimum helium shell mass models. *Astrophys. J.* **719**, 1067–1082 (2010).

90. Collins, C. E. et al. Helium as a signature of the double detonation in Type Ia supernovae. *Mon. Not. R. Astron. Soc.* **524**, 4447–4454 (2023).

91. Boos, S. J., Townsley, D. M. & Shen, K. J. Type Ia supernovae can arise from the detonations of both stars in a double degenerate binary. *Astrophys. J.* **972**, 200 (2024).

92. Shen, K. J., Boos, S. J. & Townsley, D. M. Almost all carbon/oxygen white dwarfs can host double detonations. *Astrophys. J.* **975**, 127 (2024).

## Acknowledgements

We thank S. Geier for their insightful comments during the study. J.M. was supported by funding from a Science and Technology Facilities Council (STFC) studentship. I.P. acknowledges support from The Royal Society through a University Research Fellowship (URF/R1/231496). D.J. acknowledges support from the Agencia Estatal de Investigación del Ministerio de Ciencia, Innovación y Universidades (MCIU/AEI) and the European Regional Development Fund (ERDF) with reference PID-2022-136653NA-I00 (<https://doi.org/10.13039/501100011033>). D.J. also acknowledges support from the Agencia Estatal de Investigación del Ministerio de Ciencia, Innovación y Universidades (MCIU/AEI) and the European Union NextGenerationEU/PRTR with reference CNS2023-143910 (<https://doi.org/10.13039/501100011033>). This research received funding from the European Research Council under the European Union's Horizon 2020 research and innovation programme no. 101002408 (MOS100PC). S.T. acknowledges support from the Netherlands Research Council NWO (grant VIDI 203.061). A.B. is a Postdoctoral Fellow of the Natural Sciences and Engineering Research Council (NSERC) of Canada. The study was based on observations collected at the European Organisation for Astronomical Research in the Southern Hemisphere under ESO programme 113.27QU. The Isaac Newton Telescope and the William Herschel Telescope are operated on the island of La Palma by the Isaac Newton Group of Telescopes in the Spanish Observatorio del Roque de los Muchachos of the Instituto de Astrofísica de Canarias. The study was also based on observations made with the Nordic Optical Telescope, owned in collaboration by the University of Turku and Aarhus University, and operated jointly by Aarhus University, the University of Turku and the University of Oslo, representing Denmark, Finland and Norway, the University of Iceland and Stockholm University at the Observatorio del Roque de los Muchachos, La Palma, Spain, of the Instituto de Astrofísica de Canarias. The data presented here were obtained in part with ALFOSC, which is provided by the Instituto de Astrofísica de Andalucía (IAA) under a joint agreement with the University of Copenhagen and NOT. In addition, this research was based on observations made with the NASA/ESA Hubble Space Telescope obtained from the Space Telescope Science Institute, which is operated by the Association of Universities for Research in Astronomy, Inc., under NASA contract NAS 5-26555. These observations are associated with programme 16642.

## Author contributions

J.M. and R.P. carried out most of the modelling and analysis and wrote the majority of the paper. S.S. performed spectral fitting for the ultraviolet data. A.S.R. performed MESA modelling for accurate stellar compositions. I.P. and P.-E.T. supervised the project. D.J. played an integral part in obtaining spectra of the target. G.N., M.M., S.T., A.B. and T.C. provided much insight and many discussions throughout all stages of the project. All authors contributed with comments to the writing of the paper.

## Competing interests

The authors declare no competing interests

## Additional information

**Supplementary information** The online version contains supplementary material available at <https://doi.org/10.1038/s41550-025-02528-4>.

**Correspondence and requests for materials** should be addressed to James Munday.

**Peer review information** *Nature Astronomy* thanks Dongdong Liu and the other, anonymous, reviewer(s) for their contribution to the peer review of this work.

**Reprints and permissions information** is available at [www.nature.com/reprints](http://www.nature.com/reprints).

**Publisher's note** Springer Nature remains neutral with regard to jurisdictional claims in published maps and institutional affiliations.

**Open Access** This article is licensed under a Creative Commons Attribution 4.0 International License, which permits use, sharing,

adaptation, distribution and reproduction in any medium or format, as long as you give appropriate credit to the original author(s) and the source, provide a link to the Creative Commons licence, and indicate if changes were made. The images or other third party material in this article are included in the article's Creative Commons licence, unless indicated otherwise in a credit line to the material. If material is not included in the article's Creative Commons licence and your intended use is not permitted by statutory regulation or exceeds the permitted use, you will need to obtain permission directly from the copyright holder. To view a copy of this licence, visit <http://creativecommons.org/licenses/by/4.0/>.

© The Author(s) 2025